Available online at www.sciencedirect.com
ScienceDirect
Applied Surface Science 253 (2007) 6394–6399
applied surface science
www.elsevier.com/locate/apsusc

Numerical modeling of short pulse laser interaction with Au nanoparticle surrounded by water

Alexey N. Volkov, Carlos Sevilla [1], Leonid V. Zhigilei *

Department of Materials Science and Engineering, University of Virginia, USA

Available online 3 February 2007

Abstract

Short pulse laser interaction with a metal nanoparticle surrounded by water is investigated with a hydrodynamic computational model that includes a realistic equation of state for water and accounts for thermoelastic behavior and the kinetics of electron–phonon equilibration in the nanoparticle. Computational results suggest that, at laser fluences close to the threshold for vapor bubble formation, the region of biological damage due to the laser-induced thermal spike and the interaction of the pressure wave with internal cell structures can be localized within short distances from the absorbing particle comparable to the particle diameter. This irradiation regime is suitable for targeted generation of thermal and mechanical damage at the sub-cellular level.

PACS : 78.20.Bh; 47.11.−j; 61.80.Az; 64.60.Ht

Keywords: Computer modeling; Nanoparticles; Cell targeting; Laser damage

1. Introduction

Short pulse laser irradiation of absorbing nanoparticles embedded in a transparent medium provides a method for targeted deposition of laser energy with a sub-micron resolution and serves as a basis for a number of emerging biomedical applications. In particular, it has been demonstrated that laser irradiation of gold or silver nanoparticles attached to gene markers and delivered to specific cells can be used for selective killing of cancer cells [1,2] or bacteria [3]. Similar approach has been proposed for biological imaging, when optoacoustic signals generated by nanoparticles help to differentiate small tumors from normal tissue [4]. In the area of drag delivery, doping the walls of the microcapsules with metal nanoparticles opens a way for remote release of encapsulated material into specific cells by targeting metal nanoparticles with near-infrared laser irradiation [5,6].

While the number of biomedical applications based on light-absorbing nanoparticles is growing, the understanding of the channels of energy transfer from nanoparticles to the surrounding transparent medium and the processes responsible for cell damage/death remains limited and, for the most part, relies on qualitative estimations based on the solution of the heat conduction equation [1,5,7]. At the same time, experimental observations suggest that the cell damage is typically associated with generation of vapor bubbles around the absorbing nanoparticles [1–3]. Recent investigation performed for femtosecond laser excitation and time-resolved X-ray probing of gold nanoparticles demonstrates that the vapor bubble formation exhibits a threshold dependence on laser fluence and the onset of the bubble formation strongly affects the rate of the heat transfer from the nanoparticle [8].

A reliable computational modeling of laser interaction with metal nanoparticles in a transparent medium, therefore, should go beyond the analysis of the heat transfer and should include an adequate description of the coupled thermal and mechanical processes in the nanoparticle and the surrounding medium, as well as the dynamic phase changes leading to the bubble formation. Relevant hydrodynamic modeling has been reported for laser-induced generation of bubbles and pressure waves around an absorbing melanosome particle in an aqueous

* Corresponding author.
E-mail address: lz2n@virginia.edu (L.V. Zhigilei).
[1] Present address: Department of Biomedical Engineering, University of Rochester, USA.

0169-4332/$ – see front matter © 2007 Published by Elsevier B.V.
doi:10.1016/j.apsusc.2007.01.112

medium [9–11]. Molecular dynamics simulations have been used to obtain a qualitative information on the microscopic mechanisms of short pulse laser damage to an absorbing particle embedded in a transparent medium [12] and to investigate the dynamics of the explosive phase transformation in a water layer adjacent to a hot metal surface [13].

In this work we describe a computational model developed for investigation of laser interaction with metal nanoparticles surrounded by water, critically review the applicability of several approximations commonly used in hydrodynamic modeling, and present the results of the simulations performed for a gold nanoparticle in water irradiated by a femtosecond laser pulse. The kinetics of the phase transformation in the water layer adjacent to the nanoparticle, generation of a pressure wave and evolution of the temperature distribution are studied with the focus on the potential implications for thermal and mechanical damage of cell structures. The simulations are performed for moderate laser fluences, when the temperature is below or only slightly above the critical temperature of water and the radius of the laser-induced bubble (as expected from results reported in Ref. [8]) is on the order of the radius of the metal nanoparticle.

2. Computational model

The system considered in the model is a spherical metal particle of initial radius R_p^0 surrounded by water. Laser irradiation is absorbed only by the particle with water assumed to be transparent. The heat and mass transfer in water is assumed to be spherically symmetric and is described by equations formulated in spherical coordinates r, θ, φ, where r is the distance to the center of the particle, θ and φ are the longitudinal and latitudinal angles:

$$\frac{\partial \rho}{\partial t} + \frac{\partial(\rho v_r)}{\partial r} + \frac{2}{r}\rho v_r = 0, \tag{1}$$

$$\rho\left(\frac{\partial v_r}{\partial t} + v_r\frac{\partial v_r}{\partial r}\right) = -\frac{\partial p}{\partial r} + \frac{\partial \tau_{rr}}{\partial r} + \frac{2}{r}\frac{2\tau_{rr} - \tau_{\theta\theta} - \tau_{\varphi\varphi}}{2}, \tag{2}$$

$$\rho\left(\frac{\partial \varepsilon}{\partial t} + v_r\frac{\partial \varepsilon}{\partial r}\right) = -\frac{\partial q_r}{\partial r} - (p - \tau_{rr})\frac{\partial v_r}{\partial r} - \frac{2}{r}\left[\left(p - \tau_{rr} + \frac{2\tau_{rr} - \tau_{\theta\theta} - \tau_{\varphi\varphi}}{2}\right)v_r + q_r\right], \tag{3}$$

where ρ, v_r, ε and p are the density, the component of the velocity vector in r-direction, the specific internal energy and the pressure of the fluid; τ_{rr}, $\tau_{\theta\theta}$ and $\tau_{\varphi\varphi}$ are the diagonal components of the viscous stress tensor which are described by the Newtonian fluid model; q_r is the component of the heat flux vector in r-direction which is described by the Fourier's law:

$$\tau_{rr} = \frac{4}{3}\mu\left(\frac{\partial v_r}{\partial r} - \frac{v_r}{r}\right), \quad \frac{2\tau_{rr} - \tau_{\theta\theta} - \tau_{\varphi\varphi}}{2} = 2\mu\left(\frac{\partial v_r}{\partial r} - \frac{v_r}{r}\right), \quad q_r = -\kappa\frac{\partial T}{\partial r}, \tag{4}$$

where μ, κ, and T are the viscosity, the heat conductivity, and the temperature of the fluid. The second viscosity is assumed to be zero.

Under conditions considered in this work, the continuum model represented by Eqs. (1)-(4) is applied for the description of the nanoscale flow of liquid, two-phase liquid–vapor mixture, and vapor bubble formed around the particle. For the vapor bubble, we assume that the high-pressure vapor (several MPa and more) is in near-equilibrium state with the adjacent liquid and, despite the small size of the vapor region, the continuum description still provides a realistic description of the physical behavior of the system.

In order to solve Eqs. (1)–(3) it is necessary to define the thermal $p = p(\rho, T)$ and caloric $\varepsilon = \varepsilon(\rho, T)$ equations of state. In this work, EOS recommended for general and scientific use by the International Association for the Properties of Water and Steam (IAPWS) under the document IAPWS95 [14] is used. This EOS is valid for both liquid water and water vapor for temperatures below 1273 K, which is significantly higher than the critical temperature of water, $T_c = 647$ K. Similar to Ref. [10], the liquid to vapor phase transition is described using the Maxwell rule applied under assumption that in the two-phase region of the phase diagram the state of the system is an equilibrium mixture of liquid and vapor. For a given average density ρ and temperature T of the mixture, we find the equilibrium densities of liquid $\rho_l(T)$ and vapor $\rho_v(T)$. Under the liquid–vapor coexistence curve (where $T < T_c$ and $\rho_v(T) < \rho < \rho_l(T)$) the pressure is assumed to be equal to its equilibrium value $p = p(\rho_l(T), T)$ and the energy is defined as $\varepsilon = (1 - \beta)\varepsilon(\rho_l(T), T) + \beta\varepsilon(\rho_v(T), T)$, where $\beta = \alpha\rho_v(T)/\rho$ is the mass fraction of the vapor and $\alpha = (\rho_l(T) - \rho)/(\rho_l(T) - \rho_v(T))$ is its volume fraction. Although this approach results in the appearance of a two-phase region of a finite thickness instead of a well-defined vapor bubble with a sharp liquid–vapor interface, the evolution of energy and pressure is still correctly captured by the model (see example in Ref. [10]).

The heat conductivity in the two-phase region is defined as $\kappa = (1 - \bar{\alpha})\kappa_l(T) + \bar{\alpha}\kappa_v(T)$ where $\kappa_l(T)$ and $\kappa_v(T)$ are the heat conductivities of liquid and vapor at the saturation curve, $\bar{\alpha} = \alpha/\alpha_{lim}$ at $\alpha \le \alpha_{lim}$ and $\bar{\alpha} = 1$ otherwise. The parameter α_{lim} is introduced to account for the fact that the "effective" heat conductivity of the vapor with some fraction of liquid droplets is close to the heat conductivity of pure vapor. The viscosity in the two-phase region is defined in the same way as the heat conductivity. In order to find the heat conductivity and viscosity of water along the saturation curve, the data from recent IAPWS releases [15,16] is used.

For the metal nanoparticle, the laser excitation and electron–phonon equilibration are described with the two-temperature model (TTM) [17]. The electron temperature, T_e, the lattice temperature, T_a, and pressure, p_w, are assumed to have uniform distributions throughout the particle. The homogeneous pressure inside the particle arises from thermal stresses and the elastic deformation is described by the Hook's law. The equations for the pressure and lattice energy in the particle can

be then written as follows:

$$\frac{\mathrm{d}p_\mathrm{w}}{\mathrm{d}t} = -\frac{K}{V_\mathrm{p}}\frac{\mathrm{d}V_\mathrm{p}}{\mathrm{d}t} + K\alpha\frac{\mathrm{d}T_\mathrm{a}}{\mathrm{d}t}, \qquad m_\mathrm{p}C_\mathrm{a}\frac{\mathrm{d}T_\mathrm{a}}{\mathrm{d}t}$$
$$= V_\mathrm{p}G(T_\mathrm{e} - T_\mathrm{a}) - 4\pi R_\mathrm{p}^2 q_\mathrm{w} + p_\mathrm{w}\frac{\mathrm{d}V_\mathrm{p}}{\mathrm{d}t}, \tag{5}$$

where $V_\mathrm{p} = (4/3)\pi R_\mathrm{p}^3$ and $m_\mathrm{p} = \rho_\mathrm{p}V_\mathrm{p}$ are the volume and mass of a particle with radius R_p and density ρ_p, $q_\mathrm{w} = q_r(R_\mathrm{p}, t)$ is the heat flux at the particle surface, C_a is the lattice specific heat, G is the electron–phonon coupling constant, K is the bulk modulus, $\alpha = 3\alpha_\mathrm{th}$, and α_th is the linear thermal expansion coefficient. Adding the equation for the electron temperature T_e, one can write the following equations determining the particle parameters R_p, T_a and T_e:

$$\left(\frac{1}{V_\mathrm{p}} + \frac{\alpha p_\mathrm{w}}{m_\mathrm{p}C_\mathrm{a}}\right)4\pi R_\mathrm{p}\frac{\mathrm{d}R_\mathrm{p}}{\mathrm{d}t}$$
$$= -\frac{1}{K}\frac{\mathrm{d}p_\mathrm{w}}{\mathrm{d}t} + \frac{\alpha}{m_\mathrm{p}C_\mathrm{a}}(V_\mathrm{p}G(T_\mathrm{e} - T_\mathrm{a}) - 4\pi R_\mathrm{p}^2 q_\mathrm{w}), \tag{6}$$

$$(m_\mathrm{p}C_\mathrm{a} + \alpha p_\mathrm{w}V_\mathrm{p})\frac{\mathrm{d}T_\mathrm{a}}{\mathrm{d}t}$$
$$= V_\mathrm{p}G(T_\mathrm{e} - T_\mathrm{a}) - 4\pi R_\mathrm{p}^2 q_\mathrm{w} + \frac{p_\mathrm{w}V_\mathrm{p}}{K}\frac{\mathrm{d}p_\mathrm{w}}{\mathrm{d}t}, \tag{7}$$

$$m_\mathrm{p}C_\mathrm{e}(T_\mathrm{e})\frac{\mathrm{d}T_\mathrm{e}}{\mathrm{d}t} = V_\mathrm{p}G(T_\mathrm{a} - T_\mathrm{e}) + \pi R_\mathrm{p}^2 I_\mathrm{L}(t), \tag{8}$$

where $C_\mathrm{e}(T_\mathrm{e}) = \bar{C}_\mathrm{e}T_\mathrm{e}$ is the specific heat of the electrons, $I_\mathrm{L}(t) = F_\mathrm{L}\exp(-(t-3t_\sigma)^2/2t_\sigma^2)/\sqrt{2\pi}t_\sigma$ the intensity of the absorbed laser irradiation, $t_\sigma = t_\mathrm{L}/2\sqrt{2\ln 2}$, F_L and t_L are the absorbed laser fluence and the laser pulse duration defined as the full width at half maximum of the Gaussian temporal profile of the laser pulse. The absorption of laser radiation by a particle with a size that is less or comparable with the laser wavelength is a complex optical phenomenon that results in a particle size and laser wavelength dependent absorption spectrum, see e.g. [8]. The absorption process is not explicitly considered in this work but is accounted for through the effective absorbed laser fluence F_L defining the laser energy deposition to the particle.

Eqs. (1)–(3) and (6)–(8) are solved with the following boundary and initial conditions:

$$\text{at } r = R_\mathrm{p}: \quad v_r(R_\mathrm{p}, t) = \frac{\mathrm{d}R_\mathrm{p}}{\mathrm{d}t}, \qquad T(R_\mathrm{p}, t) = T_\mathrm{a}(t),$$
$$p(R_\mathrm{p}, t) - \tau_{rr}(R_\mathrm{p}, t) = p_\mathrm{w}(t), \tag{9}$$

$$\text{at } r = R_\mathrm{e}: \quad \rho(R_\mathrm{e}, t) = \rho^0, \quad v_r(R_\mathrm{e}, t) = 0, \quad T(R_\mathrm{e}, t) = T^0, \tag{10}$$

$$\text{at } t = 0: \quad \rho(r, 0) = \rho^0, \quad v_r(r, 0) = 0, \quad T(r, 0) = T^0,$$
$$R_\mathrm{p}(0) = R_\mathrm{p}^0, \quad T_\mathrm{a}(0) = T^0, \quad T_\mathrm{e}(0) = T^0, \tag{11}$$

where R_e is the distance from the particle center to the external boundary of the computational domain and ρ^0 is the liquid density which corresponds to the initial temperature T^0 and pressure p^0. The boundary conditions defined by Eq. (10) are adequate until the compressive pressure wave reaches the external boundary at $r = R_\mathrm{e}$.

Eqs. (1)–(3) are solved numerically with the help of a splitting method. The convective part is solved by the Richtmayer or FLIC TVD schemes described in Ref. [18] and the diffusion part is solved by the central difference scheme. Eqs. (6)–(8) are solved by the improved Euler method. The computational method as a whole has second order of approximation in time and space.

The simulations of the gold nanoparticle–water system, discussed in the next section, are performed with the following parameters used in Eqs. (1)–(11): $\rho_\mathrm{p} = 19{,}300\ \mathrm{kg/m^3}$, $C_\mathrm{a} = 143.6\ \mathrm{J/(kg\ K)}$, $\bar{C}_\mathrm{e} = 0.003679\ \mathrm{J/(kg\ K^2)}$, $G = 2.1 \times 10^{16}\ \mathrm{W/(K\ m^3)}$ [19], $\alpha_\mathrm{th} = 15 \times 10^{-6}\ \mathrm{(1/K)}$, $K = 220 \times 10^9\ \mathrm{Pa}$, $T^0 = 310\ \mathrm{K}$, $p^0 = 10^5\ \mathrm{Pa}$. The initial particle radius R_p^0, the laser fluence F_L, and the pulse duration t_L are varied as follows, $R_\mathrm{p} = 25$–$200\ \mathrm{nm}$, $F_\mathrm{L} < 100\ \mathrm{J/m^2}$, $t_\mathrm{L} = 0.1$–$1\ \mathrm{ps}$.

3. Results and discussion

Typical distributions of the pressure and temperature in water around a particle with an initial radius of 50 nm irradiated by a 200 fs laser pulse with an absorbed fluence of 60 J/m^2 are shown in Fig. 1. The pressure plots indicate that a pressure wave with a smooth profile propagates away from the particle. This observation is in contrast with results reported in Ref. [10], where the emission of a shock wave with a steep front is predicted for absorbing particles in an aqueous medium irradiated by picosecond and nanosecond laser pulses.

A special investigation demonstrated that the model represented by Eqs. (1)-(4) predicts the formation of discontinuities at the shock wave front when viscosity and heat conductivity become small enough. It was found that the width of the front of the shock wave in water (12–20 nm in Fig. 1a) is defined by the values of the viscosity and heat conductivity used in the simulations. At the length scales considered in this work the finite width of the front of the shock wave is significant, highlighting the fact that the viscosity is an important factor in the considered problem.

Propagation of the pressure wave has almost no effect on the temperature distribution in water, which changes due to the heat conduction from the metal particle (Fig. 1b). The evolution of the density and temperature of water at the particle surface is shown in Fig. 2 along with saturation curve obtained from the IAPWS95 EOS. The vaporization at the particle surface starts at $t \approx 23$ ps and a layer of pure vapor is formed by $t \approx 84$ ps. The total amount of the vaporized material in this simulation remains relatively small and the effect of the vaporization process on the temperature profiles is insignificant.

The results of the simulations performed at different values of the absorbed laser fluence predict that, for the particle with radius $R_\mathrm{p}^0 = 50\ \mathrm{nm}$, the temperature in the vicinity of the metal surface reaches the boiling temperature at normal pressure ($T = 373\ \mathrm{K}$) at $F_\mathrm{L} = 18\ \mathrm{J/m^2}$ and the critical temperature at $F_\mathrm{L} = 72\ \mathrm{J/m^2}$. At higher absorbed fluences, a continuous transition from liquid to vapor without liquid–vapor coexistence takes place near the

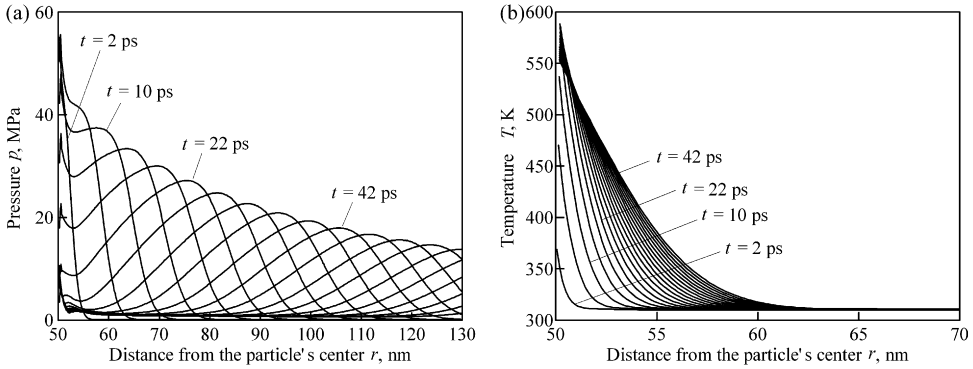

Fig. 1. Distributions of pressure p (a) and the temperature T (b) in water at every 4 ps after 2 ps. Simulation is performed with Model 1, $F_L = 60$ J/m^2, $t_L = 200$ fs, and $R_p^0 = 50$ nm.

surface of the particle, as apparent from the thermodynamic trajectory shown in Fig. 2 for fluence $F_L = 80$ J/m^2. The variation of the pulse duration within a range below the characteristic time of electron–phonon equilibration in the gold particle, ~30 ps [20], does not affect the results of the simulations.

In order to determine the extent to which the results of the simulations are affected by the kinetics of electron–phonon equilibration, thermoelastic response of the particle material, and the choice of the EOS for water, a number of simulations are performed with three simplified models listed in Table 1. The full model used in calculations discussed above is referred to as Model 1. Model 2 refers to the case when the thermoelastic response of the particle to the laser heating is not included, i.e. Eqs. (6) and (7) are solved with $\alpha_{th} = 0$ and 1/K = 0. In Model 3, the kinetics of the electron–phonon equilibration in the metal particle is not accounted for and TTM is replaced by one-temperature model (OTM), i.e. the term $m_p G(T_e - T_a)$ in Eq. (7) is replaced by the term $\pi R_p^2 I_L(t)$. Finally, in Model 4, calculation are performed with the Stiffened gas EOS [21], $\varepsilon = C_v T + p_\infty/\rho$, $p = \rho C_v(\gamma - 1)T - p_\infty$, which is widely used in modeling of liquid–gas flows including bubble formation problems. Parameters of the Stiffened gas EOS are assumed to be $\gamma = 2.79$, $p_\infty = 8.26 \times 10^9$ Pa and $C_v = 1497$ J/(kg K). With these parameters, the values of density, speed of sound, the specific heat at constant pressure calculated from the Stiffened gas EOS coincide with the values predicted by IAPWS95 EOS at temperature T^0 and pressure p^0. The use of a different set of parameters recommended in Ref. [21], $\gamma = 4$ and $p_\infty = 6 \times 10^8$ Pa, results in larger discrepancies between the predictions of Models 1 and 4 as compared to the parameters adopted in this work.

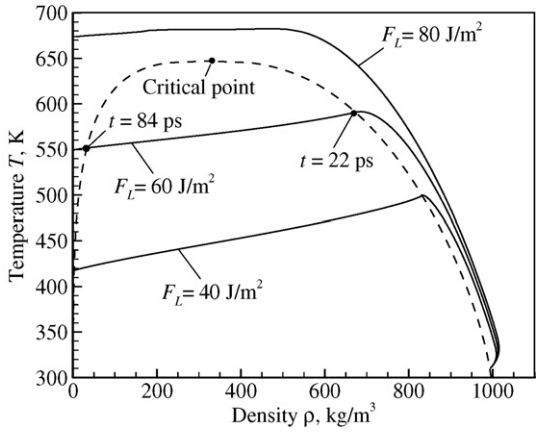

Fig. 2. Saturation curve of water (dashed curve) and parameters of water at the surface of the particle for three values of the absorbed fluence F_L. Simulations are performed with Model 1, $t_L = 200$ fs, and $R_p^0 = 50$ nm.

Computational results obtained with the help of the four models are compared in Fig. 3. One can see that the choice of the model has a profound effect on the pressure distributions. The neglect of the finite time need for the energy transfer from the excited electrons to the lattice in Model 3 results in a rapid increase of the particle lattice temperature T_a and a build up of a very high pressure near the particle at the initial stage of the process ($t < 10$ ps). The pressure wave emitted from the particle is much stronger and is generated more quickly with Model 3 as compared to other models. The values of pressure predicted with a rigid particle that does not expand with temperature, Model 2, are somewhat smaller as compared with the complete Model 1. A relatively weak effect of the thermoelasticity on the pressure increase is related to a weak electron–phonon coupling and small overall linear thermal expansion of the particle that did not exceed 0.5% in the simulation. The shapes of the pressure profiles obtained with the Stiffened gas EOS are qualitatively similar to those obtained with IAPWS95 EOS, but the maximum values of pressure are more than twice higher than the ones predicted with IAPWS95 EOS.

The temperature distributions predicted by Models 1–3, based on IAPWS95 EOS, are defined almost entirely by the heat conduction from the particle, with a very small contribution from the pressure wave (Fig. 3b). On the contrary,

Table 1
Computational models used in calculations

Model number	EOS	Electron–phonon equilibration	Particle elasticity
1	IAPWS95	Yes—TTM	Yes
2	IAPWS95	Yes—TTM	No
3	IAPWS95	No—OTM	Yes
4	Stiffened gas	Yes—TTM	Yes

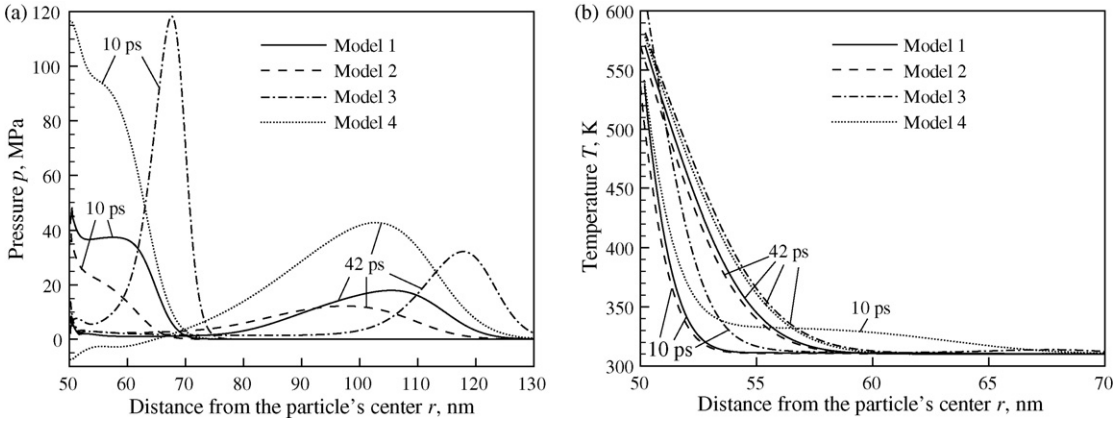

Fig. 3. Distributions of pressure p (a) and temperature T (b) in water at 10 ps and 42 ps for Models 1–4 (see Table 1). In all simulations $F_L = 60$ J/m^2, $t_L = 200$ fs, $R_p^0 = 50$ nm.

the propagation of the pressure wave in the Model 4 using the Stiffened gas EOS, is accompanied by a considerable temperature increase. The shoulder in the temperature distribution shown for 10 ps correlates with the location of the pressure wave, whereas at 40 ps the pressure wave is located outside the area shown in Fig. 3b. The linear size Δr of the near-particle layer where the temperature exceeds the normal boiling temperature for water, $T_b = 373$ K, has very weak dependence on whether the thermoelastic behavior of the particle material is included or not. At the same time, the difference between the values of Δr obtained with the help of Models 1 and 4, based on different EOS, increases with time during the simulations.

The comparison of the results predicted by Models 1–4 indicates that the models based on a simple analytic Stiffened gas EOS or not accounting for the kinetics of the electron–phonon equilibration are not appropriate for simulation of short (femto- or picosecond) pulse laser interaction with a metal nanoparticle immersed in an aqueous medium. The thermoelastic behavior of the absorber material has a considerable influence on the pressure evolution during the initial stage of the process, $t < 20$ ps, but does not affect the temperature distribution in water. It is also found what the computational results do not change in any significant way if a simplified model in which the thermal expansion of the particle is described by a simple equation $R_p(t) = R_p^0 \exp(\alpha_{th}(T_a(t) - T^0))$ and the evolution of pressure, p_w in Eq. (5), is not considered.

Connecting the results of the simulations discussed above to the possible mechanisms of targeted cell damage in the biomedical applications of nanoparticles [1–3], we can use rough estimations of the critical values of temperature that may lead to protein denaturation and mechanical stresses that may induce a mechanical damage in cell structures. Assuming that the rate of the thermal damage of proteins, cells and biological tissues can be described by the Arrhenius equation, and extrapolating experimental data obtained on the timescale of seconds and minutes to nano- and picoseconds, the temperature range of 370–470 K has been estimated for thermal denaturation occurring on the timescale of hundreds of picoseconds [22]. Using the normal boiling temperature $T_b = 373$ K as a conservative (lower-end) estimate of the temperature that would cause ultrafast thermal damage, we calculate the width of the layer Δr_{th}^* where the protein denaturation may take place during the short laser-induced thermal spike around the

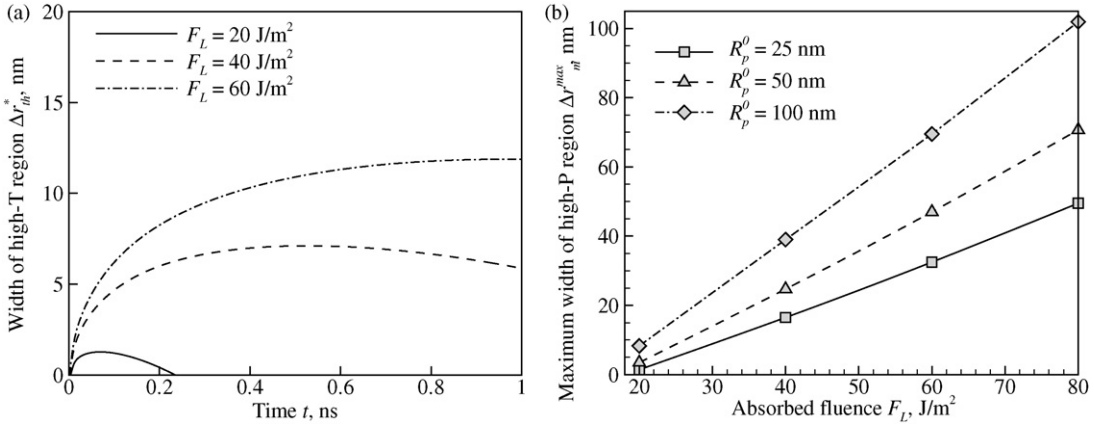

Fig. 4. The width of the regions of potential thermal (a) and mechanical (b) damage to biological structures adjacent to the absorbing particle. The time evolution of the high temperature region Δr_{th}^* (where $T > 373$ K) is shown for $R_p^0 = 50$ nm and three values of the absorbed fluence F_L in (a). The width of the high-pressure region Δr_m^{max} (where $p > 20$ MPa) is shown for several particle radii R_p^0 in (b). Simulations are performed with Model 1 and $t_L = 200$ fs.

absorbing particle (Fig. 4a). In the range of fluences studied in this work, the temperature spike is localized within tens of nanometers from the particle surface and lasts less than a nanosecond, suggesting that biological damage from the thermal effects would occur only in the immediate vicinity of the particle.

An alternative damage mechanism that should be considered is the mechanical destruction of cell structure by high tensile stresses. Analysis of the simulation results indicates that, due to the formation of a vapor bubble, the pressure waves emitted from the particle do not have any significant tensile component, Fig. 1a (significant tensile stresses are observed only in simulations performed with the Stiffened gas EOS, where vaporization is not taken into account, see Fig. 3a). Partial reflection of the compressive pressure wave from internal sub-cellular structures may, however, result in the generation of the tensile stresses and associated cell damage. Assuming that tensile stresses exceeding 1 MPa can induce local cell damage and taking the value of the reflection coefficient at an internal sub-cellular interface as 0.05 [9], we can estimate that the photomechanical damage may occur in the region where the amplitude of the compressive pressure wave exceeds 20 MPa. The width of a region of the potential photomechanical damage, $\Delta r_{\mathrm{m}}^{\max}$, is shown for different particle sizes and absorbed fluences in Fig. 4b. While the high-pressure region is somewhat larger than the high-temperature region shown in Fig. 4a, the mechanical damage is still predicted to be localized at short distances comparable to the particle diameter. At higher laser fluences generation of a larger vapor bubble may cause more extensive photomechanical damage [1–3,9,23,24]. Nevertheless, the results presented in this work suggest that within a relatively broad range of absorbed laser fluences, close to the threshold for vapor bubble formation, both photothermal and photomechanical damage produced by irradiation of metal nanoparticles can be localized at the sub-cellular (sub-micron) scale, providing attractive opportunities for biomedical applications.

4. Summary

Computational model is developed for simulation of short pulse laser interaction with a metal nanoparticle surrounded by water. The hydrodynamic model describes the heat and mass transfer in the system by the one-dimensional Navier–Stokes equations and includes a realistic equation of state for water, TTM representation of the kinetics of electron–phonon equilibration in the metal nanoparticle, as well as a description of the thermoelastic response of the particle material. One-temperature model of heating of the absorbing particle and the simplified Stiffened gas EOS are found to be inappropriate for simulations of femto- and picosecond laser pulse irradiation of a metal nanoparticle surrounded by water. Computational results suggest that, at laser fluences close to the threshold for vapor bubble formation, the region of biological damage due to the thermal spike and the interaction of the laser-induced pressure wave with internal cell structures can be localized within short distances from the absorbing particle comparable to the particle diameter. This irradiation regime provides an opportunity for selective generation of localized biological damage at the sub-cellular level.

Acknowledgement

Financial support of this work is provided by the National Science Foundation through the Thermal Transport and Thermal Processes Program of the Chemical and Transport Systems Division (Award no. CTS-0348503).

References

[1] C.M. Pitsillides, E.K. Joe, X. Wei, R.R. Anderson, C.P. Lin, Biophys. J. 84 (2003) 4023.
[2] D. Lapotko, E. Lukianova, M. Potapnev, O. Aleinikovac, A. Oraevsky, Cancer Lett. 239 (2006) 36.
[3] V.P. Zharov, K.E. Mercer, E.N. Galitovskaya, M.S. Smeltzery, Biophys. J. 90 (2006) 619.
[4] J.A. Copland, M. Eghtedari, V.L. Popov, N. Kotov, N. Mamedova, M. Motamedi, A.A. Oraevsky, Mol. Imag. Biol. 6 (2004) 341.
[5] A.G. Skirtach, C. Dejugnat, D. Braun, A.S. Susha, A.L. Rogach, W.J. Parak, H. Möhwald, G.B. Sukhorukov, Nano Lett. 5 (2005) 1371.
[6] A.G. Skirtach, A.M. Javier, O. Kreft, K. Köhler, A.P. Alberola, H. Möhwald, W.J. Parak, G.B. Sukhorukov, Angew. Chem. Int. Ed. 45 (2006) 4612.
[7] M. Hu, G.V. Hartland, J. Phys. Chem. B 106 (2002) 7029.
[8] V. Kotaidis, C. Dahmen, G. von Plessen, F. Springer, A. Plech, J. Chem. Phys. 124 (2006) 184702.
[9] M. Strauss, P.A. Amendt, R.A. London, D.J. Maitland, M.E. Glinsky, C.P. Lin, M.W. Kelly, Proc. SPIE 2975 (1997) 261.
[10] J.M. Sun, B.S. Gerstman, B. Li, J. Appl. Phys. 88 (2000) 2352.
[11] E. Faraggi, B.S. Gerstman, J.M. Sun, J. Biomed. Opt. 10 (2005) 064029.
[12] L.V. Zhigilei, B.J. Garrison, Proc. SPIE 3254 (1998) 135.
[13] Y. Dou, L.V. Zhigilei, N. Winograd, B.J. Garrison, J. Phys. Chem. A 105 (2001) 2748.
[14] W. Wagner, A. Pruß, J. Phys. Chem. Ref. Data 31 (2002) 387.
[15] Revised Release on the IAPS Formulation 1985 for the Thermal Conductivity of Ordinary Water Substance (International Association for the Properties of Water and Stream, 1998), http://www.iapws.org/.
[16] Revised Release on the IAPS Formulation 1985 for the Viscosity of Ordinary Water Substance (International Association for the Properties of Water and Stream, 2003), http://www.iapws.org/.
[17] S.I. Anisimov, B.L. Kapeliovich, T.L. Perel'man, Sov. Phys. JETP 39 (1974) 375.
[18] E.F. Toro, Riemann Solvers and Numerical Methods for Fluid Dynamics, Springer, Berlin, 1999.
[19] J. Hohlfeld, S.-S. Wellershoff, J. Güdde, U. Conrad, V. Jähnke, E. Matthias, Chem. Phys. 251 (2000) 237.
[20] Z. Lin, L.V. Zhigilei, Proc. SPIE 6261 (2006) 62610U.
[21] G. Perigaud, R. Saurel, J. Comp. Phys. 209 (2005) 139.
[22] G. Hüttmann, R. Birngruber, IEEE J. Sel. Top. Quantum Electron. 5 (1999) 954.
[23] D.O. Lapotko, Lasers Surg. Med. 38 (2006) 240.
[24] A. Vogel, V. Venugopalan, Chem. Rev. 103 (2003) 577.